

This article has been published in Journal of Materials Processing Technology. The final publication is available at Elsevier via <https://doi.org/10.1016/j.jmatprotec.2019.116551>

Meso-scale modelling of semi-solid deformation in aluminum foundry alloys: Effects of feeding and microstructure on hot tearing susceptibility

F. Sheykh-jaberi¹, S.L. Cockcroft¹, D.M. Maijer¹, A.B. Phillion²

¹Department of Materials Engineering, The University of British Columbia, Vancouver, Canada

²Department of Materials Science and Engineering, McMaster University, Hamilton, Canada

Keywords: Hot tearing; aluminum alloys; meso-scale modelling; eutectic and dendritic microstructure; semi-solid constitutive behaviour

Abstract

In the context of hot tearing susceptibility, the semi-solid constitutive behaviour of two commercially important foundry aluminum alloys at high solid fraction has been simulated. The numerical methodology combines solid mechanics, computational fluid dynamics, and microstructure modelling, *i.e* a meso-scale multi-physics approach. Feedable and un-feedable domains with different microstructures including equiaxed globular, equiaxed dendritic, and combined dendritic and eutectic were developed. Considering that it is the combined effects of a lack of liquid feeding and limited semi-solid ductility that contribute to hot tearing formation, the effect of feeding and mechanical deformation are studied and discussed. The model demonstrates that the microstructure type and the eutectic formation also have a considerable effect on the liquid channels pressure drop and semi-solid bulk stress and strain, and consequently on hot tearing.

I. Introduction

Shape casting provides the most cost-effective way for manufacturing aluminum components of complex geometry for a variety of applications in the automotive and aerospace industries. Recently, there has been substantial interest in replacing conventional foundry alloys with high-strength alternatives. These new alloys provide desirable weight savings but also increase

manufacturing costs. For the high-strength B206 alloy, a recently developed variant in the Al-Cu 206 family with strict limits on Fe and Ti, one of the main issues, as highlighted by (Eskin, 2008) is the occurrence of hot tearing, also known as solidification cracking, due to a long solidification range and limited eutectic content. As identified by (Major and Sigworth, 2006), although the strict limit on Ti permits the use of an inoculant to grain refine and form globular grains, dendritic grains can still form and hot tearing will still occur. As a result, using B206 in geometrically complex castings represents an exciting engineering opportunity as well as a significant processing challenge.

Simulations have, for many years, played an important role in predicting hot tearing susceptibility of an alloy or a casting. Modelling the semi-solid constitutive behaviour and thus hot tearing is a challenging problem because of the large difference in viscosity, and by extension deformation behaviour, between the liquid and solid phases. In order to overcome the limits introduced by volume averaging, and based on experiments highlighting the importance of the granular nature of solidifying alloys such as performed by (Gourlay and Dahle, 2007), multi-physics meso-scale models have now been created whereby the semi-solid material is simulated using separate solid and liquid elements. These models take into account macroscopic fields (stress and strain), as well as microstructural features (grain size and shape) to predict both deformation of the solid grains and flow in the intergranular region. (Ferrez, 2001) proposed the first meso-scale multi-physics solidification model to simulate the two-dimensional behaviour of solid grains assuming circular and rigid geometry. (Martin et al., 2006) extended this work to incorporate deformable grains, but still only considered interactions between grains that were due to solid-solid contact; the influence of the surrounding liquid was neglected. (Dijkstra et al., 2004) extended this “regular grains” geometric arrangement by using a set of hexagons to model liquid feeding within a semi-solid. As first proposed by (Mathier et al., 2007), a more realistic model of grain structure can be achieved by substituting the regular arrangement of grains with an irregular one using a Voronoi diagram. This idea was improved by (Vernede et al., 2006; Vernède and Rappaz, 2007) in an Al-Cu binary alloy by considering rounded corners to accurately predict grain coalescence. Using a similar approach, (Phillion et al., 2008) estimated the mechanical behaviour of an semi-solid Al-Mg alloy by taking into account the effect of microstructural features (solid fraction, porosity, and grain size) and considering the liquid as a compliant solid.

The concept of granular modelling for solidification was in recent years extended to 3D. (Zaragoci et al., 2012) used X-ray micro-tomographic images of semi-solid Al-Cu to generate geometry for 3D semi-solid finite element simulations, showing that during the tensile testing a maximum strain rate value of 0.1 s^{-1} is found in the liquid pockets while stresses are quite heterogeneously distributed in the solid with a maximum value $\sim 7 \text{ MPa}$. (Sistaninia et al., 2012) developed a comprehensive 3D hydro-mechanical granular model to compute the solidification of large mushy zones, followed by concurrent deformation, intergranular feeding, and crack formation simulations to accurately predict the semi-solid stress-strain behaviour of metallic alloys. (Zareie Rajani and Phillion, 2018) extended Sistaninia's approach to fusion welding of Al alloys, taking into account the effects of both large thermal gradients and mechanical constraints provided by the base metal. (Feng, Yi and Phillion, 2018), using a volume average approach to simulate solidification of individual grains, were able to apply this technique to steel alloys where the microstructure is largely dendritic and not globular. The above set of studies have provided much mechanistic insight into the interplay between deformation and fluid flow leading to hot tearing. However, microstructure based on the Voronoi polyhedrons is representative of primary alloy solidification with globular grain morphology. Foundry alloys show a dendritic and/or eutectic structure that requires additional considerations for meso-scale multi-physics modelling of hot tearing.

Recently (Sheykh-jaberi et al., 2019) reported on the semi-solid tensile properties of B206 along with the common A356 Al-Si foundry alloy. The results indicated that the semi-solid yield stress and ductility were strongly linked to small variation in solid fraction. Further, for B206 the tensile behaviour was sensitive to microstructure length scale whereas it was not in A356. This study complements the prior experimental observations by utilizing the multi-physics meso-scale modelling approach to investigate the microstructural phenomena that are active during semi-solid deformation of foundry aluminium alloys. The effects of grain shape (globular vs. dendritic) and solidification mode (primary vs. eutectic) are simulated to gain new insight into the factors that differentiate hot tearing susceptibility between B206 and A356.

II. Model Description

The multi-physics meso-scale models directly simulates semi-solid deformation at the scale of the microstructure via an approach known as Fluid/Structure Interactions (FSI) where fluid flow

affects compliant structures, which in turn affect the fluid flow. The commercial software Abaqus™ was used for the FSI simulations with the structural and fluid equations solved independently and the interfacial loads and boundary conditions exchanged after achieving a converged increment. The model was developed to predict the semi-solid behaviour of the B206 and A356 alloys without and with eutectic, respectively.

a. Model Geometry

The 2D microstructure model that forms the basis of the simulations is based on the granular method for semi-solids (Vernede et al., 2006) and extends earlier work (Phillion et al., 2008) to additionally consider the effects of dendritic and/or eutectic grains on semi-solid constitutive behaviour in the high solid fraction (0.85-0.98) regime, and ultimately hot tearing. The basis of the geometry the approximation of grains via polygons based on the Voronoi diagram (Nygårds, 2003) of a random set of nuclei, resulting in irregular grain arrangement within a representative volume element (RVE). Note that although the simulation is conceptually 2D, a 3D geometry was utilized as the CFD implementation within Abaqus™ consists of only 3D elements. For this reason, the 2D domain was extruded by 10 μm in the thickness direction.

To simulate semi-solid deformation in *equiaxed-globular microstructure*, each Voronoi polygon is reduced in size independently of the others by moving the coordinates of each vertex towards the nucleation point until the area of this new grain relative to the area of the Voronoi polygon is equal to the solid fraction of interest. The excluded material is considered to be liquid. The resulting geometry contains a random configuration of grains fully surrounded by continuous films of liquid. The channels between the grains vary in thickness depending on the size of the grains, and the distance between the grain nuclei. Fig. 1(a) shows a Voronoi diagram, while Fig. 1(b) shows the modified diagram providing semi-solid geometry with $f_s=0.9$. In Fig. 1(a), the dark lines (marker i) represent grain boundaries. In Fig. 1(b) and all subsequent figures the dark lines (marker ii) represent liquid.

To simulate *equiaxed-dendritic* microstructure, each Voronoi polygon representing an equiaxed-globular grain is replaced by a clover leaf shape to mimic a dendrite in 2D (Bayani et al., 2014). The shapes are equivalent in area to their polygon counterpart but rotated up to 45° to create random orientation; the remaining material represents the liquid phase. Fig. 2 shows the semi-solid microstructure at (a) low, (b) moderate, and (c) high solid fraction. As can be seen, an increase in solid fraction results first in grain impingement and followed by the formation of

isolated liquid pockets. This represents the percolation effect that plays a major role in assessing hot tearing susceptibility (Mathier et al., 2004). Because of the use of a 2D domain, concurrent percolation of both the solid and liquid phases across the RVE is not possible.

Finally, as shown in Fig. 2(d), a structure that is *dendritic/eutectic* can be simulated by adding globular grains to surround each primary dendritic grain. For these simulations, the eutectic is added once the primary dendritic grains achieve a solid fraction corresponding to the value that exists just prior to the eutectic transformation. For A356, the value is $f_s=0.5$ (Kaufman and Rooy, 2004). The resulting microstructure displays an uneven configuration consisting of primary dendritic grains and eutectic. The use of both primary and eutectic grains allows for different mechanical properties in each region.

b. Material Properties

The input properties for the liquid phase were density ($\rho = 2500kg \cdot m^{-3}$) and viscosity ($\mu = 1.4mPa \cdot s$) (Kaufman and Rooy, 2004). The input properties for the solid phase were elastic modulus (E), Poisson's ratio (ν), and yield stress (σ_y). Although polycrystalline aluminum is known to have isotropic properties, anisotropic elastic constants ($E_x = E_y = 50GPa; E_z = 5e5GPa$, and $\nu_{xy} = 0.33; \nu_{xz} = \nu_{yz} = 0$) were utilized in order to minimize displacements in the thickness (z) direction thus making possible a 2D FSI simulation using the 3D geometric constraint imposed by the Abaqus™ CFD solver. The choice of σ_y is critical for predicting the semi-solid constitutive behaviour. For B206, the temperature-dependent semi-solid σ_y values measured during compression tests by (Mohseni et al., 2016) were utilized. In addition to temperature, σ_y depends strongly on chemical composition. For the primary grains of A356, σ_y values measured by (Singer and Cottrell, 1947) on an Al-1.6 wt.%Si alloy were utilized as this corresponds almost exactly to the maximum solid solubility of Si in Al. For the eutectic grains, the values measured by (Singer and Cottrell, 1947) on an Al-12wt.%Si alloy were utilized as this corresponds closely to the Al-Si eutectic composition. The specific values are shown in Figure 3, both (a) as a function of liquid fraction and (b) a function of temperature. As can be seen, when plotted with respect to liquid fraction, B206 has a higher yield strength as compared to either phase of A356 at liquid fractions below 0.15 (solid fractions above 0.85).

c. Model Implementation

A script file was written in the Abaqus-Python programming language to create and mesh an RVE $2 \times 3 \text{ mm}^2$ containing 600 grains. The mesh size was $\sim 10 \text{ }\mu\text{m}$. Voronoi diagrams of the

domain were obtained using the Voro++ computational library (Rycroft, 2009). The solid grains were provided with elastic-fully plastic-rate independent constitutive behaviour. Liquid flow was simulated as laminar and incompressible. During each simulation, deformation was applied to both the left and right surfaces of the RVE. These were each linked to reference points that were displaced by applying a strain rate of 0.001s^{-1} . The simulation was performed for 10 s or until issues of mesh distortion resulted in the solver exceeding the convergence limit.

Both Well-Fed (WF) and Un-Fed (UF) boundary conditions were considered. The WF case represents a scenario analogous to shape casting with a well-designed riser and gating system. For the liquid, the boundary (top surface) through which feeding can occur was set at a fixed pressure ($P = 0$) and unknown fluid flux ($\phi \neq 0$) allowing for liquid flow into the RVE. The other three surfaces were closed ($P \neq 0, \phi = 0$). For the solid grains, the bottom surface was fixed in the y -direction while one node at the middle of the bottom surface was fixed in the x -direction to constrain displacement. The UF case represents the scenario analogous to a semi-solid tensile test where metal has been heated from the solid state. As deformation is localized to the hottest part of the sample, external feeding is not possible thus all surfaces are closed ($P \neq 0, \phi = 0$). The solid grains used the same boundary conditions as the WF case. The choice of boundary conditions also affects the microstructure model geometry. For the case of a well-fed RVE, the liquid remained percolated, *i.e.* all the liquid channels were connected, at all fraction solids. For the case of an unfed equiaxed-globular RVE, continuous solid networks have been found to form above $f_s > 0.93$ (Vernede et al., 2006); the model geometry was modified to account for this behavior. Grain impingement and thus the formation of a continuous solid network occurs naturally in the dendritic and dendritic-eutectic RVEs as shown in Figure 2(c) and (d).

Figure 4 shows four RVEs, each at $f_s = 0.95$. Comparing first the equiaxed-globular WF and UF geometries it can be seen that the former, Figure 4(a), consists of solid grains surrounded by continuous liquid channels that exist as a result of solidification whereas the latter, Figure 4(b), consists of disconnected liquid channels indicative of local melting at the grain boundaries occurring upon heating from room temperature. The liquid in the UF equiaxed-dendritic RVE, Figure 4(c), appears as small liquid pockets as opposed to channels that are partially isolated and partially interconnected to other dendrites. Finally, the liquid in the UF dendritic-eutectic RVE, Figure 4(d), consists of much larger pockets and is further connected as compared to the unfeedable equiaxed-globular and equiaxed-dendritic RVEs.

III. Results

A series of meso-scale simulations using the developed approach have been performed on the microstructure models in order to investigate semi-solid deformation in a multi-physics context as a function of solid fraction. The modelling approach provides the stress in the solid grains as well as the pressure distribution throughout the liquid channels. The model is able to show stress concentrations, fluid flow and its localization. For each simulation, the maximum strain (ε_{max}) is assumed to occur at the point where the model convergence limit is reached.

WF Simulations

Figure 5 shows an example output from one set of simulations of semi-solid B206 having globular microstructure and using WF boundary conditions. This figure shows specifically (a) the evolution in average pressure drop within the liquid channels as a function of solid fraction, (b) ε_{max} for each of the four solid fractions, $f_s = 0.85, 0.90, 0.95,$ and 0.98 , and (c-e) contour plots of the von Mises stress at four levels of strain for the simulation performed at $f_s=0.95$. Note that deformation is tensile and horizontal. Further, although with increasing solid fraction the size of liquid channels gets smaller, it should be noted that in the feedable domain, even at very high solid fraction the liquid channels remain interconnected.

Beginning with Figure 5(a), it can be seen that in all cases, the pressure drop first increases sharply to accelerate fluid in response to the deformation. At the relatively low solid fractions of 0.85 and 0.90, the pressure drop then gradually reduces as a result of the good feeding and in the case of $f_s=0.85$ returns to nearly zero. Thus, in these cases the deformation is predominantly accommodated within the liquid channels. However, the pressure evolution is highly solid fraction dependent; at high values of solid fraction the channels are too narrow to allow for even small amounts of fluid flow prior to them becoming so distorted that the computation no longer converges. The corresponding ε_{max} for each simulation can be seen in Figure 5(b); the change in solid fraction from 0.85 to 0.98 leads to a decrease in ε_{max} from $\approx 8 \times 10^{-3}$ to a value less than 1×10^{-3} . Finally, the resulting stress contours at $f_s=0.95$, Figures 5(c-e) show that although the stress in the solid grains increases with an increase in the applied strain, it remains very low because the pressure drop in the liquid is small and on the order of a few kPa (Figure 5(a)). Specifically, these contours show that at small strains, $\varepsilon = \varepsilon_{max}/10$, the fluid velocity is increasing thus resulting in stress development in the solid grains. With an increase to $\varepsilon = \varepsilon_{max}/2$, and then finally to $\varepsilon = \varepsilon_{max}$ it is seen that larger areas of the RVE are subjected to a pressure drop

and stress variation. As there is no continuous solid network from one side of the domain to the other, the stress develops only as a result of the liquid pressure. As long as the pressure drop in the liquid is not in the range of σ_y , the liquid pressure cannot plastically deform the solid grains. Further, the stress remains well below any cavitation pressure that could nucleate voids and cause hot tearing to occur.

UF Simulations

The results from the un-fed meso-scale multi-physics models of the equiaxed-globular B206, the equiaxed-dendritic B206 as well as the dendritic-eutectic A356 are shown in Figures 6 to 8. It is seen that the overall semi-solid deformation behaviour and pressure drop greatly depends on the structure of the solid, the size of the liquid channels, and their morphology. A comparison of ϵ_{max} for each grain morphology as a function of solid fraction is given in Figure 6. It is clear from this figure that when un-fed boundary conditions are used, the maximum permissible strain is quite low irrespective of the microstructure and approximately a factor of ten smaller than what was seen in the UF cases, Figure 5(b). Although the values are similar, the trends are quite different with the equiaxed-globular B206 showing a distinct minima at $f_s = 0.9$ whereas the equiaxed-dendritic B206 show little permissible strain until $f_s = 0.98$. The dendritic-eutectic A356 shows relatively little difference in ϵ_{max} between the different solid fractions.

A summary of the evolution in average fluid pressure during tensile deformation is shown in Figure 7. As expected, the liquid pressure drop is highly dependent on both the solid fraction and the grain morphology. The UF equiaxed-globular B206 RVE, Figure 7(a), shows a 2-3 order of magnitude higher pressure drop in all cases than the corresponding WF case. For example, at $f_s = 0.95$, the UF pressure drop was 260 kPa whereas the feedable pressure drop was 1.2 kPa. The observed differences between the individual curves in Figure 7(a) are a result of the percolation of the various phases. While at $f_s = 0.85$ and $f_s = 0.98$ there are wide liquid channels and considerable solid bridging to allow for either fluid flow or deformation, respectively, at $f_s = 0.90$ and $f_s = 0.95$ the permeability is limited and yet the grain bridging is minimal. This results in a high pressure drop as well as high stress (as will be shown below). Further, unlike the feedable case, a reduction in the pressure drop with increasing strain is not seen in Figure 7(a) since there is no fluid available to respond to the pressure gradient. Comparing the various pressure drops obtained for different microstructures, it can be seen that the grain morphology plays a significant role, as great a role as the solid fraction. For the equiaxed-dendritic B206 RVE, Figure 7(b), the highest pressure drop

(~1200 kPa) is seen at $f_s = 0.85$ whereas in the equiaxed globular case, Figure 7(a), the highest pressure drop (~260 kPa) is seen at $f_s = 0.95$. Finally, it can be seen that the pressure drop evolution for the A356 case, Figure 7(c), is very different and reaching only small values, although this might be because of the relatively low ε_{max} values as compared to the other cases.

Contour plots of the von Mises stress at ε_{max} for the three morphologies are shown in Figure 8 for $f_s = 0.95$. In all three of these cases, the stress has increased due to the fluid flow and grain deformation until input yield strength of the solid is reached. Note that as ε_{max} varies between simulation, each plot represents a different bulk strain. Due to the nature of the percolation in the different cases, there is considerable stress in-homogeneity and localization. The maximum stress is seen in the percolated grains as the load transfers throughout the RVE; there is very little stress in grains completely surrounded by liquid. In the equiaxed-globular case, Figure 8(a), very little stress has built-up and yielding has occurred in only a few ligaments between the grains. In the equiaxed-dendritic B206 case, Figure 8(b), the maximum stress is developed over a significant fraction of the RVE resulting in plastic deformation in these areas. Due to the dendritic shape, the load transfer results in high stress. Further, because of the nature of the isolated liquid pockets, the liquid pressure will drop to very low values in pockets where the stress does not develop; this can lead to pore cavitation and hot tearing. The stress distribution in the dendritic-eutectic A356, Figure 8(c), is completely different than the equiaxed-dendritic B206. In this morphology, the regions of low stress are seen to be much better interconnected, allowing for distribution of fluid to counteract deformation. This is because, given the combination of dendritic grains and circles representing eutectic, the size of the liquid pockets is much larger. Further, the regions of high stress are isolated, allowing for better strain distribution.

IV. Discussion

The results of the WF and UF equiaxed-globular B206 simulations can be examined to gain understanding of the effect of feeding on semi-solid deformation. In both cases, redistribution of the liquid to compensate the deformation is hindered by the morphology of the liquid channels and the dense packing of the grain structure. Comparing Figures 5(a) and 7(a), it can be seen that the pressure drop is quite small in the well-fed simulations, due to the existence of a liquid source that provides fluid in response to a pressure gradient. However, in the un-fed simulations, there is no external feeding and as a result, the pressure drops significantly during tensile deformation.

Overall, the pressure drop is approx. two orders of magnitude smaller in the WF case as compared to the UF case. The pressure drop is also seen to be dependent on solid fraction. In the WF case, the pressure drop is very small at low solid fractions such as 0.85. With an increase in the solid fraction, the liquid channels get narrower, as a result, the permeability becomes limited and pressure drop increases. In the UF case, the pressure drop is affected by both the thickness of the liquid channel and the number of the percolated grains. Although there are similar trends in both cases showing an increase in pressure drop with an increase in solid fraction, the effect of solid fraction on pressure drop is much more significant in the UF case as compared to the WF case because the thin liquid channels require fluid yet none is available. Interestingly, the pressure drop is quite large at $f_s = 0.95$, then decreases at $f_s = 0.98$. This is due to the fact that the solid structure has now largely percolated. The observed differences in pressure drop translate into differences in maximum strain. With feeding present, the liquid can compensate for semi-solid deformation enabling relatively large maximum strains. When the supply of liquid is cut, deformation localizes to poorly-shaped liquid channels and liquid pockets, increasing the susceptibility of a hot tear. This hypothesis is further supported through the contour plots, Figures 5(e) and 8(a) that show the presence of very little stress in the WF case and significant stress localization on the UF case. Finally, in all cases except $f_s = 0.98$ the maximum strains of WF exceeded UF by at least one order of magnitude. At the very high value of solid fraction, the percolated grains connect to each other allowing for significant solid deformation. Collectively, these simulations demonstrate the difficulty in measuring semi-solid constitutive behaviour using tensile tests. A specimen reheated to the semi-solid state with no possibility for liquid feeding will show the constitutive behaviour of the underlying solid grains, while a well-fed casting will exhibit a very different stress/strain response when deformed.

A comparison of the UF equiaxed-globular and equiaxed-dendritic B206 simulations indicate that the dendritic structure will show higher pressure drops, and lower maximum strain except at $f_s = 0.98$. When deformation is applied, the rounded shape of B206 globular grains move easily past one another, causing the pressure drop to remain small, Figure 7(a), which enables larger bulk strain. In contrast, when deformation is applied on the B206 dendrite microstructures, Figure 7(b), the liquid is trapped between dendrite arms which prevents the liquid from flowing freely, thus increasing the pressure drop. The contour plots of Figures 8(a) and (b) demonstrate this sliding ability of the globular structure as the majority of the RVE shows little stress even

without feeding. In comparison, stress is significantly distributed throughout the dendritic RVE. At $f_s = 0.98$, the larger maximum strain is a result of more significant percolation, as dendrites become more entangled with surrounding grains.

Finally, the equiaxed-dendritic B206 and dendritic-eutectic A356 simulations can be compared in order to address the effect of the eutectic constituent. It is seen that the pressure drop values for the UF A356 simulations are lower than the pressure drop values for the UF dendritic B206 cases. This is related to the shape and size of the liquid channels. In dendritic B206 they are irregular with small and isolated liquid pockets due to the existence of entangled dendrites branches. In the case of A356, the dendritic arms of the primary phase are covered with spherical eutectic thus changing the channel shape from irregular to smooth. As a result, fluid flow and permeability would be improved. The influence of the liquid channel shape on the pressure drop has been studied by several researchers (Hasan et al., 2009; Ravigururajan, 1998), where it was demonstrated that by changing the shape of the liquid channel from smooth edges to irregular with many branches, pressure drop increases. In a further study by Khajeh (Khajeh and Maijer, 2011), it was shown that the geometry of liquid channels undergoes a transition from dendritic to globular during the growth of eutectic grains and concurrently creating smoother liquid channels that are more elongated and interconnected. This previous finding is reinforced by the present microstructure model simulations. Thus, although both the equiaxed-dendritic and the dendritic-eutectic RVEs contain these liquid pockets, the shape and interconnectivity in the dendritic-eutectic case, aids in keeping the pressure drop small as well as distributing the deformation throughout the domain.

V. Conclusions

A new meso-scale multi-physics semi-solid model has been developed to study deformation and hot tearing in foundry alloys. This model has been used to investigate the effects of equiaxed-globular, equiaxed-dendritic, and dendritic-eutectic microstructure on the pressure drop in response to tensile deformation. It has been shown that:

- (1) Changing the microstructure from globular to dendritic significantly increases the pressure drop.
- (2) The formation of a eutectic microstructure can be effective in decreasing the pressure drop by changing the shape of the micro liquid channels.

It is well known that hot tearing susceptibility is enhanced in semi-solids having dendritic microstructure and limited eutectic fraction. The findings in this study demonstrate the underlying mechanisms responsible for this behaviour. It is clear from the simulation results that B206 is more susceptible to hot tearing than A356 because of its dendritic structure and thin liquid channels significantly increase the pressure drop resulting from tensile deformation. These features also increase the risk of the formation of an unfeedable mushy zone. However, hot tearing is also possible in A356, although the eutectic fraction is quite high, if feeding is limited or the deformation is large.

VI. Acknowledgements

The authors are grateful for the funding provided by the Natural Sciences and Engineering Research Council of Canada under the Automotive Partnership Canada Program, and Canadian Autoparts Toyota Inc, and for the funding provided by the Natural Sciences and Engineering Research Council of Canada and partner companies under the Strategic Project “Through-Process Modelling: Castings for Marine Energy Systems.”

VII. Figure Headings

Fig. 1: Equiaxed-globular microstructure representing (a) Fully solid geometry and (b) semi-solid geometry with liquid channels at $f_s=0.90$. The markers (i,ii, and iii) identify grains, grain boundaries, and liquid channels.

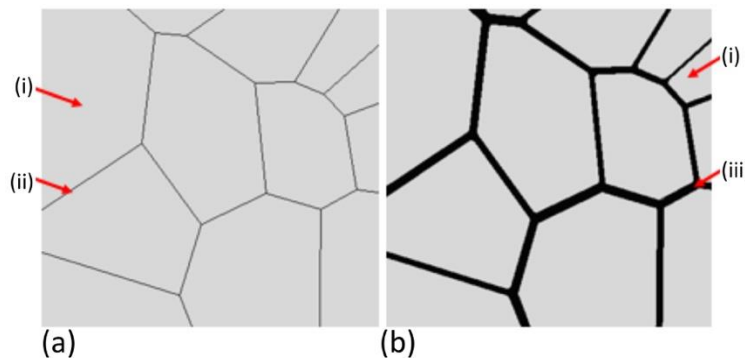


Fig. 2: (a,b,c) Equiaxed-dendritic microstructure at low, moderate, and high solid fraction showing the percolation phenomenon and the formation of isolated liquid pockets; (d) Partially eutectic microstructure showing isolated liquid pockets at $f_s=0.90$. The markers (i-v) identify primary dendritic grains, liquid, grain impingement, isolated pockets, and eutectic.

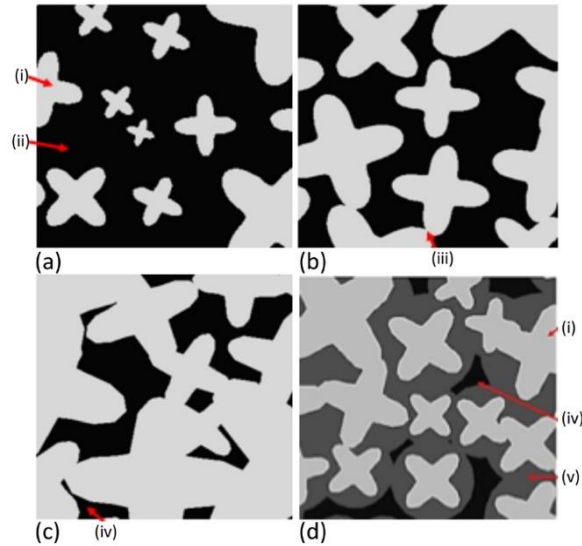


Fig. 3: (a) Fraction-liquid dependent and (b) Temperature-dependent yield stresses for B206 (Mohseni et al., 2016), Al-1.6 wt.% Si, and Al-12 wt.% Si (Singer and Cottrell, 1947).

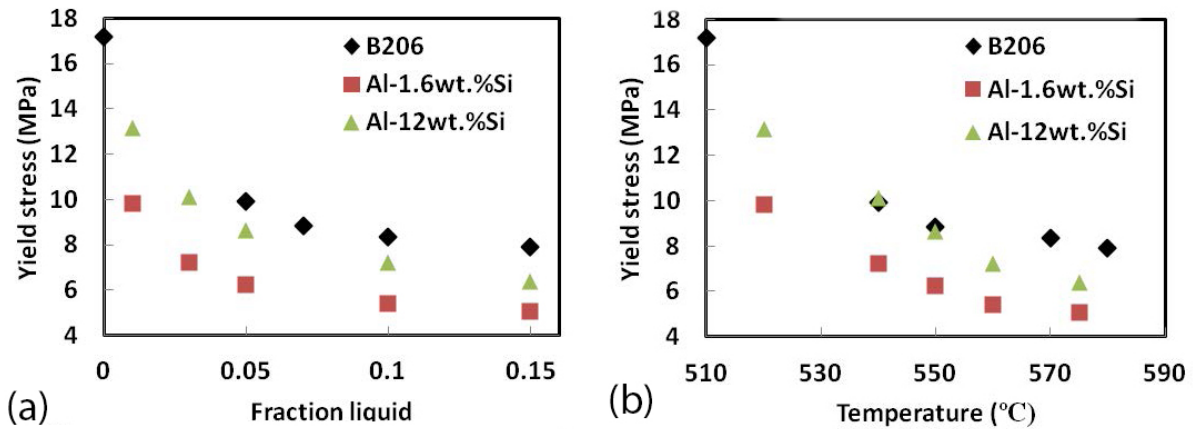
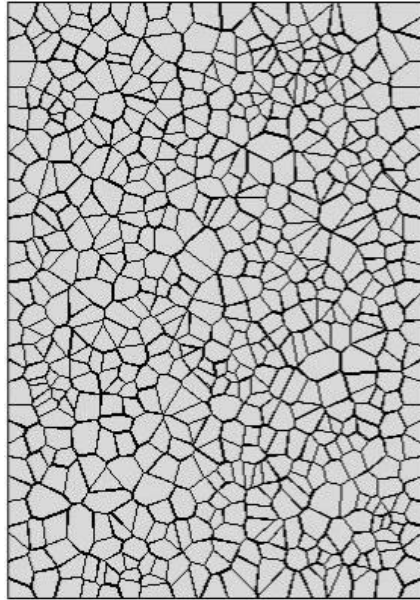
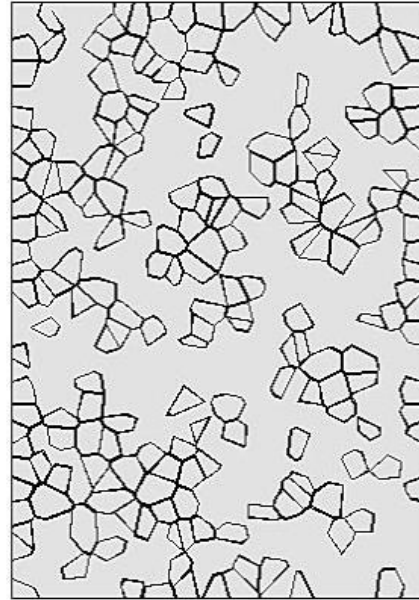


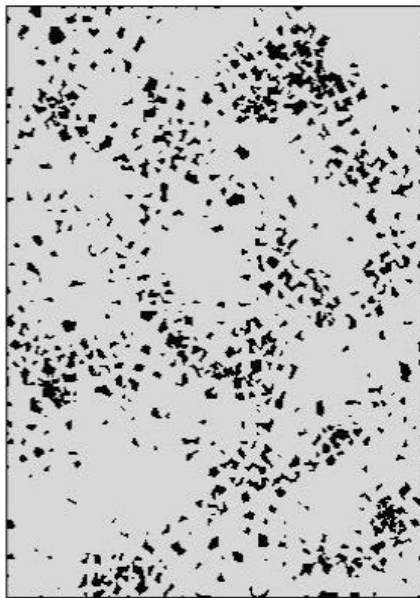
Fig. 4: Microstructure RVE at $f_s=0.95$; (a) feedable globular, (b) unfeedable globular, (c) unfeedable dendritic, and (d) unfeedable dendritic with eutectic cases. The dimensions of each RVE are $2 \times 3 \text{ mm}^2$.



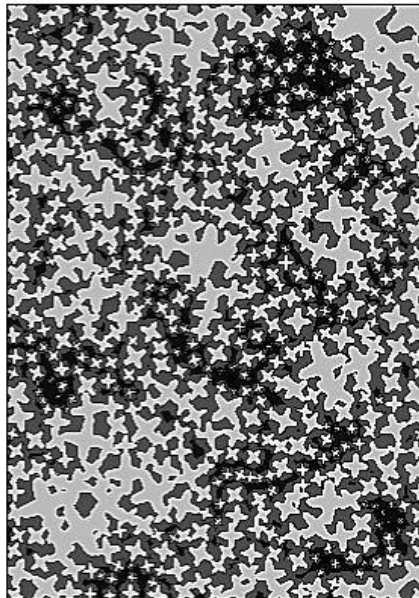
(a)



(b)



(c)



(d)

Fig. 5: Simulation results for the feedable B206 meso-scale multi-physics simulations; (a) Variation in average liquid pressure with strain at different solid fractions; (b) corresponding maximum strain as a function of solid fraction; (c-f) contour plots of the Von Mises stress $f_s=0.95$ at $\epsilon=0$, $\epsilon=\epsilon_{max}/10$, $\epsilon=\epsilon_{max}/2$, and $\epsilon=\epsilon_{max}$.

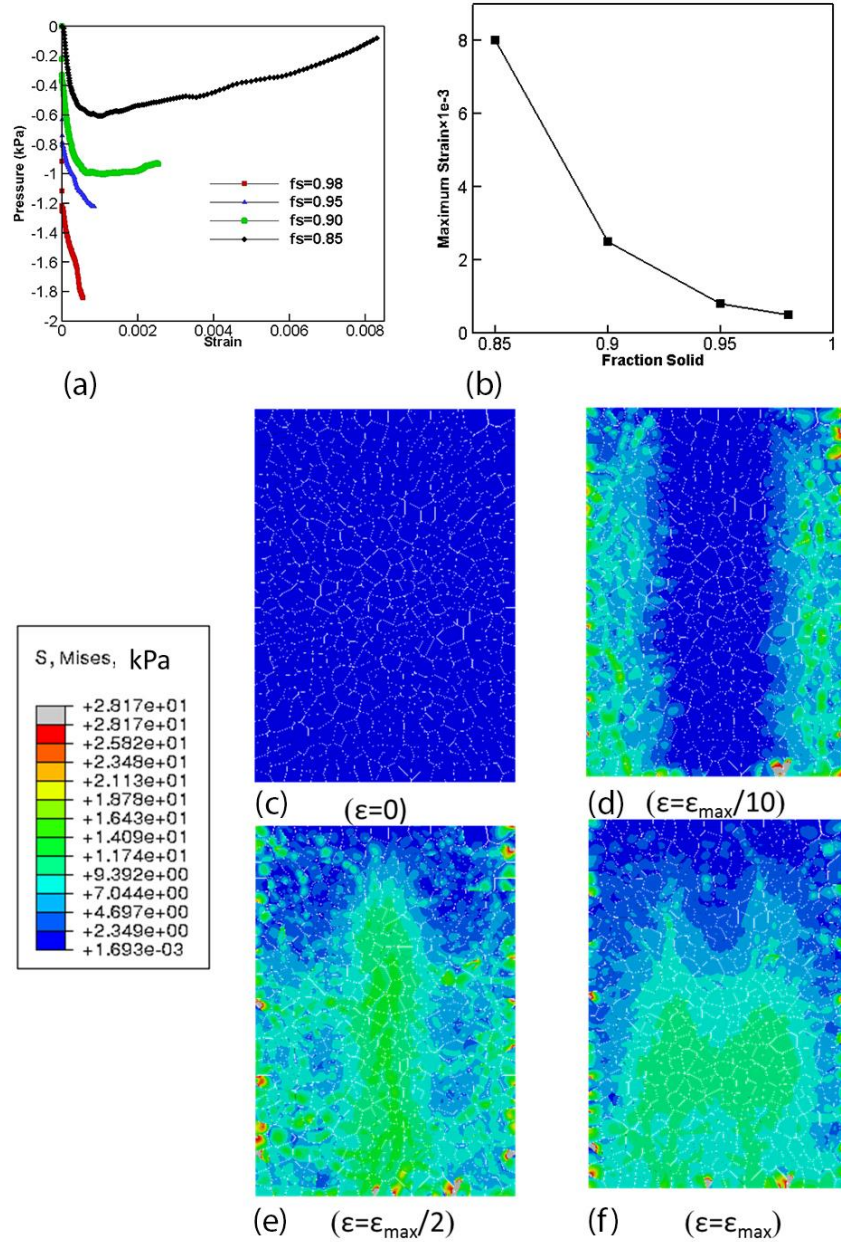


Fig. 6: Calculated maximum strain as a function of solid fraction for the un-fed globular B206, un-fed dendritic B206, and un-fed A356 simulations.

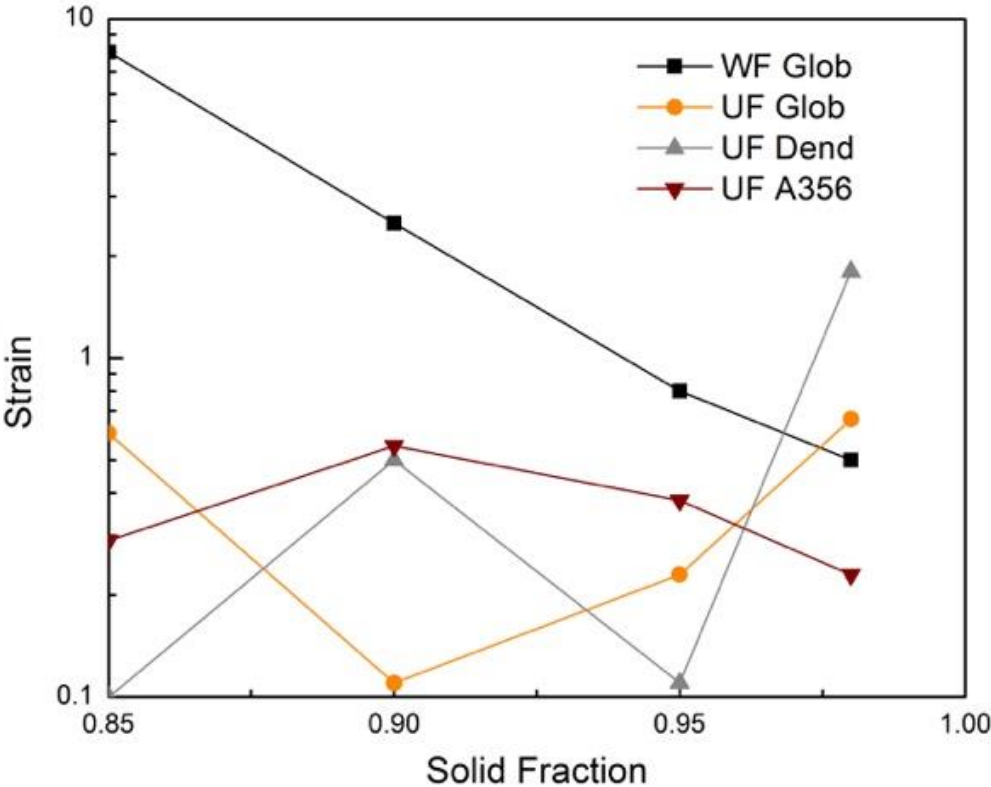
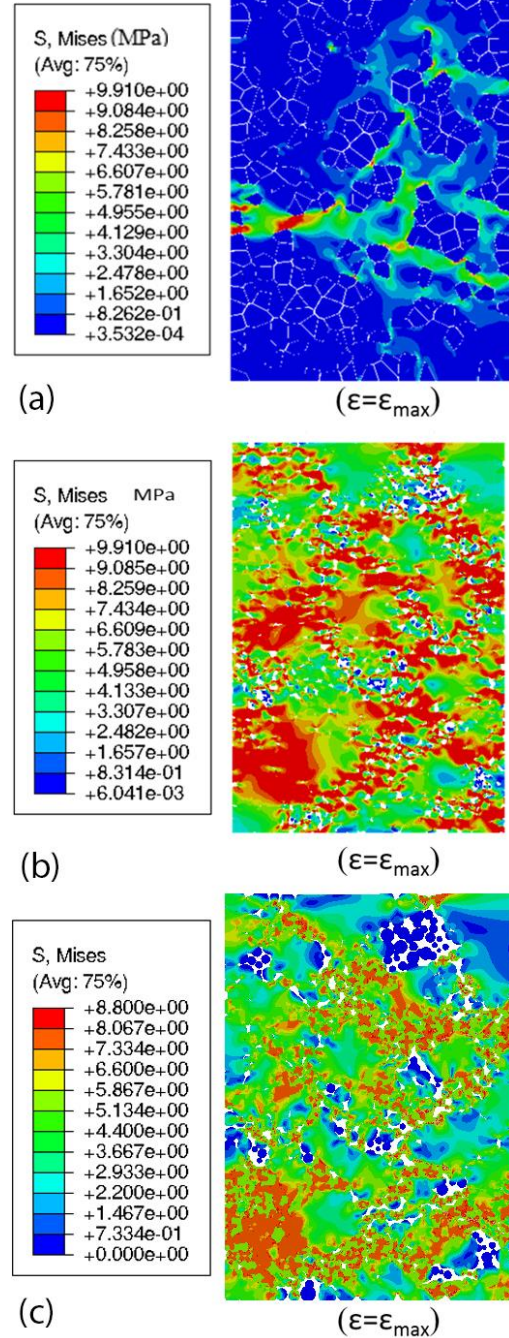
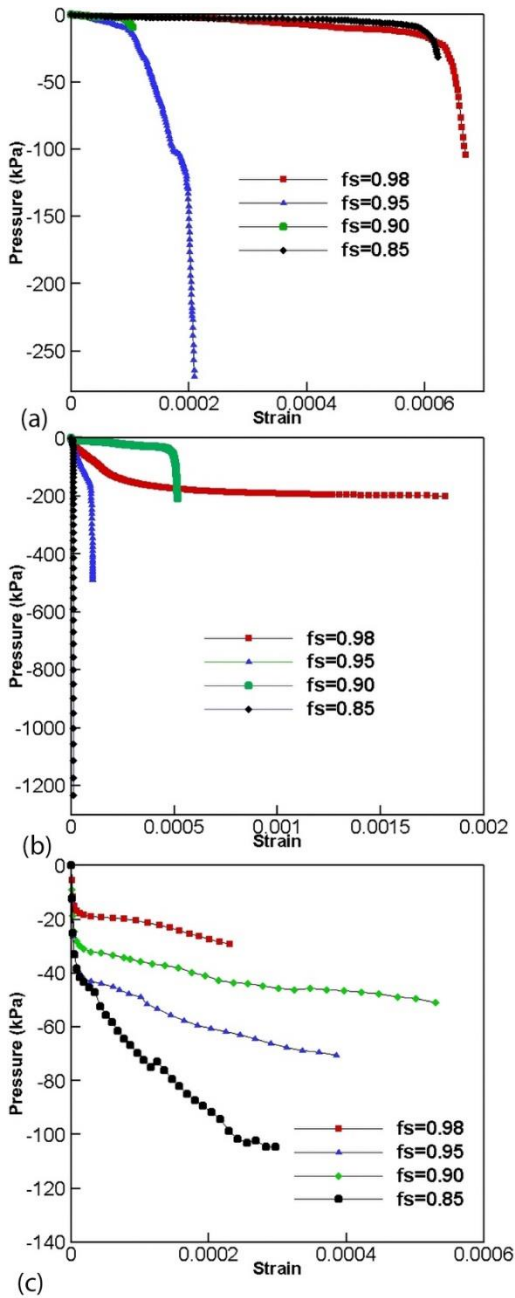


Fig. 7 (left-hand image): Variation in average liquid pressure with strain at different solid fractions for the (a) un-fed globular B206, (b) un-fed dendritic B206, and (c) un-fed A356 simulations.

Fig. 8 (right-hand image): Contour plots of the final von Mises stress at ϵ_{\max} for simulations performed at $f_s=0.95$. (a) un-fed globular B206, (b) un-fed dendritic B206, and (c) un-fed A356. The white areas indicate liquid regions where the von Mises stress not computed.



VIII. Figure Captions

Figure 1: Equiaxed-globular microstructure representing (a) Fully solid geometry and (b) semi-solid geometry with liquid channels at $f_s=0.90$. The markers (i,ii, and iii) identify grains, grain boundaries, and liquid channels.

Figure 2: (a,b,c) Equiaxed-dendritic microstructure at low, moderate, and high solid fraction showing the percolation phenomenon and the formation of isolated liquid pockets; (d) Partially eutectic microstructure showing isolated liquid pockets at $f_s=0.90$. The markers (i-v) identify primary dendritic grains, liquid, grain impingement, isolated pockets, and eutectic.

Figure 3: (a) Temperature dependent and (b) fraction liquid dependent yield stresses for B206 (Mohseni et al., 2016), Al-1.6 wt.% Si, and Al-12 wt.% Si (Singer and Cottrell, 1947).

Figure 4: Microstructure RVE at $f_s=0.95$; (a) feedable globular, (b) unfeedable globular, (c) unfeedable dendritic, and (d) unfeedable dendritic with eutectic cases. The dimensions of each RVE are $2 \times 3 \text{ mm}^2$.

Figure 5: Simulation results for the feedable B206 meso-scale multi-physics simulations; (a) Variation in average liquid pressure with strain at different solid fractions; (b) corresponding maximum strain as a function of solid fraction; (c-e) contour plots of the Von Mises stress $f_s=0.95$ at $\varepsilon=0$, $\varepsilon=\varepsilon_{max}/10$, $\varepsilon=\varepsilon_{max}/2$, and $\varepsilon=\varepsilon_{max}$.

Figure 6: Calculated maximum strain as a function of solid fraction for the un-fed globular B206, un-fed dendritic B206, and un-fed A356 simulations.

Figure 7: Variation in average liquid pressure with strain at different solid fractions for the (a) un-fed globular B206, (b) un-fed dendritic B206, and (c) un-fed A356 simulations.

Figure 8: Contour plots of the final von Mises stress at ε_{max} for simulations performed at $f_s=0.95$. (a) un-fed globular B206, (b) un-fed dendritic B206, and (c) un-fed A356.

Figure 8: Contour plots of the final von Mises stress at ε_{max} for simulations performed at $f_s=0.95$. (a) un-fed globular B206, (b) un-fed dendritic B206, and (c) un-fed A356. The white areas indicate liquid regions where the von Mises stress not computed.

IX. References

- Bayani, H., Mirbagheri, S.M.H., Barzegari, M., Firoozi, S., 2014. Simulation of unconstrained solidification of A356 aluminum alloy on distribution of micro/macro shrinkage. *J. Mater. Res. Technol.* 3, 55–70. <https://doi.org/10.1016/j.jmrt.2013.10.011>
- Dijkstra, W.O., Vuik, C., Dammers, A.J., L., K., 2004. Network Modeling of Liquid Metal Transport in Solidifying Aluminum Alloys, in: Rappaz, M., Beckermann, C., Trivedi, R. (Eds.), *Solidification Processes and Microstructures*. TMS, pp. 151–156.
- Eskin, D.G., 2008. *Physical Metallurgy of Direct Chill Casting of Al Alloys*. CRC Press.
- Feng, Yi and Phillion, A.B., 2018. A 3D Solidification Model for Steels, in: *AISTech 2018 Proceedings*. p. 7 pages.
- Ferrez, J.A., 2001. *Dynamic Triangulations for Efficient 3D Simulation of Granular Materials*, PhD Thesis. EPFL.
- Gourlay, C.M., Dahle, A.K., 2007. Dilatant shear bands in solidifying metals. *Nature* 445, 70–73. <https://doi.org/10.1038/nature05426>
- Hasan, M.I., Rageb, A.A., Yaghoubi, M., Homayoni, H., 2009. Influence of channel geometry on the performance of a counter flow microchannel heat exchanger. *Int. J. Therm. Sci.* 48, 1607–1618. <https://doi.org/10.1016/j.ijthermalsci.2009.01.004>
- Kaufman, J.G., Rooy, E.L., 2004. *Aluminum Alloy Castings: Properties, Processes, and Applications*. ASM International.
- Khajeh, E., Maijer, D.M., 2011. Permeability of dual structured hypoeutectic aluminum alloys. *Acta Mater.* 59, 4511–4524. <https://doi.org/10.1016/j.actamat.2011.03.074>
- Major, J.F., Sigworth, G.K., 2006. Chemistry/Property Relationships in AA206 Alloys. *AFS Trans.* 114, 117–128.
- Martin, C.L., Bouvard, D., Delette, G., 2006. Discrete element simulations of the compaction of aggregated ceramic powders. *J. Am. Ceram. Soc.* 89, 3379–3387. <https://doi.org/10.1111/j.1551-2916.2006.01249.x>
- Mathier, V., Drezet, J.M., Rappaz, M., 2007. Two-phase modelling of hot tearing in aluminium alloys using a semi-coupled approach. *Model. Simul. Mater. Sci. Eng.* 15, 121–134. <https://doi.org/10.1088/0965-0393/15/2/008>
- Mathier, V., Jacot, A., Rappaz, M., 2004. Coalescence of equiaxed grains during solidification. *Model. Simul. Mater. Sci. Eng.* 12, 479–490.

- Mohseni, S.M., Phillion, A.B., Maijer, D.M., 2016. Modelling the constitutive behaviour of aluminium alloy B206 in the as-cast and artificially aged states. *Mater. Sci. Eng. A* 649. <https://doi.org/10.1016/j.msea.2015.09.118>
- Nygårds, M., 2003. Microstructural Finite Element Modeling of Metals, PhD Thesis. Swedish Royal Institute of Technology.
- Phillion, A.B., Cockcroft, S.L., Lee, P.D., 2008. A three-phase simulation of the effect of microstructural features on semi-solid tensile deformation. *Acta Mater.* 56. <https://doi.org/10.1016/j.actamat.2008.04.055>
- Ravigururajan, T.S., 1998. Impact of channel geometry on two-phase flow heat transfer characteristics of refrigerants in microchannel heat exchangers. *J. Heat Transfer* 120, 485–491. <https://doi.org/10.1115/1.2824274>
- Rycroft, C.H., 2009. VORO++: A three-dimensional Voronoi cell library in C++. *Chaos*. <https://doi.org/10.1063/1.3215722>
- Sheykh-jaberi, F., Cockcroft, S.L., Maijer, D.M., Phillion, A.B., 2019. Comparison of the semi-solid constitutive behaviour of A356 and B206 aluminum foundry alloys. *J. Mater. Process. Technol.* <https://doi.org/10.1016/j.jmatprotec.2018.10.029>
- Singer, A.R., Cottrell, S.A., 1947. Properties of Al-Si alloys temperatures in the region of the solidus. *J. Institute Met.* 73, 33–54.
- Sistaninia, M., Phillion, A.B., Drezet, J.-M., Rappaz, M., 2012. A 3-D coupled hydromechanical granular model for simulating the constitutive behavior of metallic alloys during solidification. *Acta Mater.* 60. <https://doi.org/10.1016/j.actamat.2012.08.057>
- Vernède, S., Jarry, P., Rappaz, M., 2006. A granular model of equiaxed mushy zones: Formation of a coherent solid and localization of feeding. *Acta Mater.* 54, 4023–4034.
- Vernède, S., Rappaz, M., 2007. A simple and efficient model for mesoscale solidification simulation of globular grain structures. *Acta Mater.* 55, 1703–1710.
- Zaragoci, J.F., Silva, L., Bellet, M., Gandin, C.A., 2012. Numerical tensile test on a mushy zone sample, in: *Materials Science and Engineering 33*. IOP Conference Series, p. 12054.
- Zareie Rajani, H.R., Phillion, A.B., 2018. 3D multi-scale multi-physics modelling of hot cracking in welding. *Mater. Des.* 144, 45–54. <https://doi.org/10.1016/j.matdes.2018.02.007>